Geophysical Research Letters

RESEARCH LETTER
10.1029/2019GL084801

Observing Oblique Slip During Rift Linkage in Northern Afar

Alessandro La Rosa[1,2], Carolina Pagli[2], Derek Keir[1,3], Federico Sani[1], Giacomo Corti[4], Hua Wang[5], and Daniel Possee[3]

[1]Dipartimento di Scienze della Terra, Università di Firenze, Firenze, Italy, [2]Dipartimento di Scienze della Terra, Università di Pisa, Pisa, Italy, [3]Ocean and Earth Science, University of Southampton, Southampton, UK, [4]Consiglio Nazionale delle Ricerche, Istituto di Geoscienze e Georisorse, Florence, Italy, [5]Department of Surveying Engineering, Guangdong University of Technology, Guangzhou, China

Abstract Extensional plate boundaries are segmented by offsets that transfer extension between the ends of adjacent portions of the rift by linkage zones ranging in width from a few tens of kilometers to several hundreds of kilometers. However, the kinematics of linkage zones is poorly constrained as direct observations are difficult to make. Here we combine InSAR, seismicity, and structural geology data from the Afar rift to show that an active linkage zone currently connects the two offset Erta Ale and Tat Ali segments. The overall right-lateral shear between the segments is accommodated primarily by oblique left-lateral slip along faults subparallel to the rift segments but an active conjugate fault system with right-lateral slip is also present. Our results provide the first direct observational evidence that offset rift segments during continental breakup can be linked by a shear zone composed of a conjugate set of oblique slip faults.

Key Points:
- Observations of crustal deformation in the linkage zone between two rift segments in northern Afar, Ethiopia
- InSAR, seismic, and structural data show oblique slip along faults subparallel to the rift segments
- Evidences of left-lateral oblique shear within a right-lateral transfer zone caused by rift segment linkage

Supporting Information:
- Supporting Information S1
- Table S1

Correspondence to:
A. La Rosa,
alessandro.larosa@unifi.it

Citation:
La Rosa, A., Pagli, C., Keir, D., Sani, F., Corti, G., Wang, H., & Possee, D. (2019). Observing oblique slip during rift linkage in northern Afar. *Geophysical Research Letters*, *46*. https://doi.org/10.1029/2019GL084801

Received 4 AUG 2019
Accepted 5 SEP 2019
Accepted article online 12 SEP 2019

1. Introduction

During magma-rich continental rupture, magmatic and tectonic activity is accommodated at the rift axis along distinct magmatic segments (Hayward & Ebinger, 1996). Extension between offset rift segments is transferred through linkage zones whose geometry and kinematics affects the architecture of the plate boundary and may control ridge segmentation after breakup (Illsley-Kemp et al., 2018; Wetzel et al., 1993). In the oceans, transform faults have long been observed to link mid-ocean ridge segments, but non-transform offsets can also form primarily when segments are offset by less than a few tens of kilometers (Grindlay et al., 1991; Macdonald et al., 1988). In northern Iceland for example, book-shelf faulting has been invoked to explain nontransform linkage between overlapping and nearby ridge segments (Green et al., 2014).

The Afar depression results from the divergence of the Nubian, Arabian, and Somalian plates along the Red Sea, Gulf of Aden, and Main Ethiopian rift arms during the last 30 Myr (Barberi & Varet, 1970; Beyene & Abdelsalam, 2005). GPS measurements show current full spreading vectors in the southern Red Sea rift ranging from ~7 mm/year at 16°N to ~20 mm/year at 13°N in an ~N60°E direction (Figure 1a; McClusky et al., 2010). The extension is mainly focused in en echelon magmatic segments, similar in morphology and spacing to the segments observed along slow spreading mid-ocean ridges (Hayward & Ebinger, 1996; Keir et al., 2009). Geophysical and geological observations of rifting episodes in Afar and Iceland have shown that spreading at the axial magmatic segments occurs through repeated diking (e.g., Dabbahu, 2005–2010 and Krafla, 1975–1984, Wright et al., 2012) fed by crustal magma chambers and normal faulting (Pagli et al., 2014; Wright et al., 2012). However, there is no consensus on how offset magmatic rift segments interact and link.

In northern Afar, two main rift segments are present: the Erta Ale (EA) and Tat Ali (TA) segments (Figure 1a). EA is offset from TA through an ~20-km-wide zone of intense fracturing known as the Afrera Plain (AP). The AP is ~100 m below the sea level and it includes interbedded evaporitic deposits formed during past marine incursions, and young lava flows (Keir et al., 2013). The regions of lowest elevation are currently filled by Lake Afrera, which is fed mainly by hot springs. Eight years of seismicity measurements from a local seismic array have shown continuous low-to-moderate seismicity at AP (Belachew et al., 2011; Ebinger et al., 2008; Illsley-Kemp et al., 2018). The largest event during this time period was the M_L 5.1 earthquake on 2 October 2007 (Figure 1), with no indication from geodetic data of any associated magma

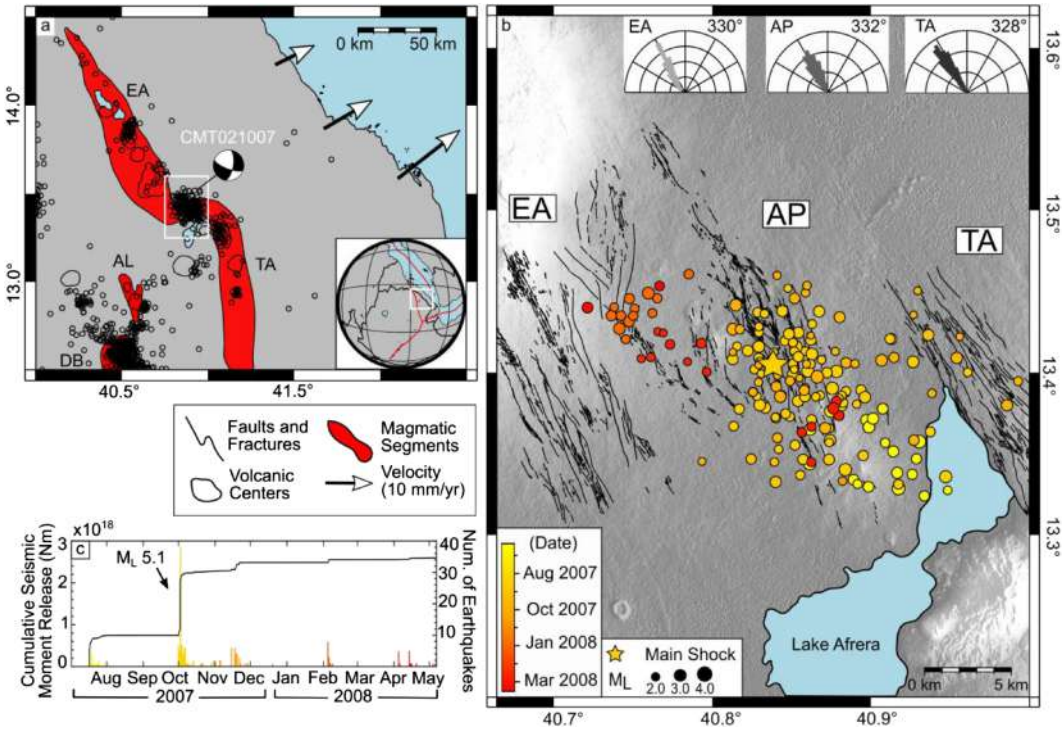

Figure 1. Tectonics and seismicity of Afar. (a) Magmatic segments in northern Afar and seismicity during 2005–2009 (black circles; Ebinger et al., 2008). Focal mechanism is from the Centroid Moment Tensor (CMT) catalogue. GPS velocities are from McClusky et al. (2010). The white box marks the location of Figure 2. (b) Relocated seismicity between July 2007 and May 2008 with faults and fractures (black lines). The rose diagrams show the faults orientations of the EA and TA rift segments and the AP offset. (c) Cumulative seismic moment release and number of earthquakes as in (b).

intrusions (Illsley-Kemp, Bull, et al., 2018; Pagli et al., 2014). In contrast, earthquake swarms along the magmatic segments such as EA segment are mainly induced by magma intrusion (Pagli et al., 2012). Based on geological, seismic, and geodetic observations, along with numerical modeling, Bonatti et al. (2017) and Illsley-Kemp, Keir, et al. (2018) argued that the deformation between the EA and TA segments is related to the early formation of an ~EW trending transform fault.

Here we combined a data set of structural, InSAR, and seismic observations from the AP to provide new constraints on the mechanisms of segment linkage. Our data show that left-lateral oblique slip along ~N-S oriented faults occurs, indicating that a nontransform zone of oblique tectonics achieves plate boundary linkage between the EA and TA rifts.

2. Data Analysis

2.1. Structural Analysis

Detailed structural mapping has been carried out through interpretation of 1-m-resolution satellite imagery (Digital Globe) and the 30-m Shuttle Radar Topography Mission (SRTM) DEM using ArcMap 10.6 and Google Earth Pro. More than 2,000 faults and fractures have been identified within the northern TA and southern EA segments and the AP. For each zone, fault strikes have been measured tip-to-tip and reported within 4° binned rose diagrams (Figures 1b and 2a). The fault system in the AP have also been further analyzed to identify different fault populations and their kinematics. Following the approach of Acocella and Korme (2002), we also made direct field measurements of opening directions on pairs of asperities across extensional fractures to evaluate the local extension direction.

Faults within EA and TA show the same regional NNW trend with structures having an average strike of N330°E and N328°E, respectively (Figure 1b). Conversely, the strike of faults and fractures in AP is not

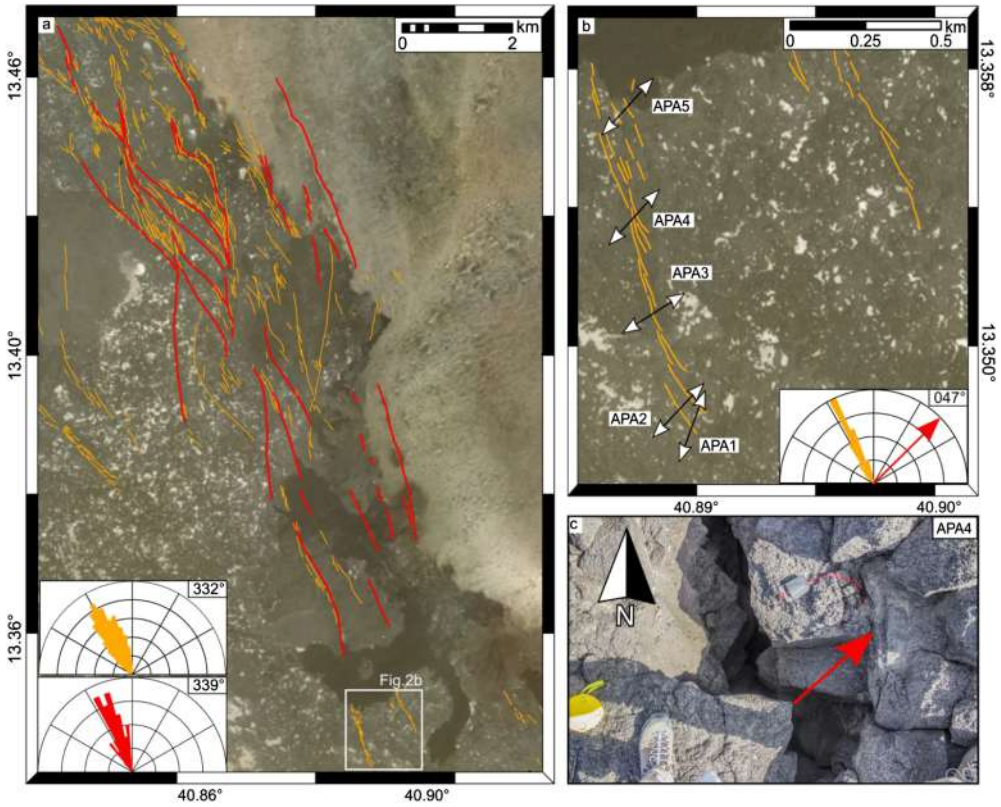

Figure 2. Structures at Afrera Plain (see Figure 1b for location). (a) Faults (red lines) and fractures (orange lines). The rose diagrams show the strikes of the structures using the same colors as in the map. (b) Field measurements of opening direction along extensional fractures. The rose diagram shows an average opening direction of N47°E, oblique to the average fractures' direction of N332°E. (c) Field observation of extensional oblique fracture formed at a fault tip (see also Figure S1 and Table S1).

homogeneous, with trends ranging between NNW-SSE and N-S with an average fault strike of ~N340° E (Figure 2a).

The fault system at AP, between latitude N13.41° and N13.45°, consists of a set of main faults connected by intricate patterns of fractures and minor faults forming a lozenge-shaped releasing bend (Figure 2a), similar to those predicted by analogue modeling of oblique extensional tectonics (McClay et al., 2002). Further to the south (Figures 2a and 2b), we carried out a field campaign covering an ~1-km^2 area at the southern end of the AP fault system. Here we observed horsetail fractures, such as observed at the termination of a shear fault, with average opening direction of N47°E on a N332° striking fault, indicating left-lateral motion (Figures 2, S1, and Table S1). Horsetail fractures form perpendicularly to the extension direction and hence the fault termination is curved with respect to the strike of the main fault (Kim et al., 2004).

2.2. InSAR Analysis

We processed four coseismic interferograms using Envisat acquisitions from one ascending (028) and three descending (278, 049, and 464) tracks. The track 464 is in I6 mode (mean incidence angle 41°), and all the other tracks are in I2 mode (mean incidence angle 23°). We formed the interferograms using the JPL/Caltech ROI_PAC software (Rosen et al., 2004) and 3-arc sec SRTM DEM (Farr et al., 2007). All the coseismic interferograms cover the area of the main shock on 2 October 2007 and the time separation between acquisitions spans different time periods, ranging from 2 to 10 months. Four interferograms, covering the preseismic and postseismic periods, were also processed to measure deformation before and after the main shock (Figure S2).

Both ascending and descending coseismic interferograms (Figures 3 and S2) show a deformation pattern with a main lobe elongated in a NNW direction with up to 3.2 cm of range increase along the satellite line

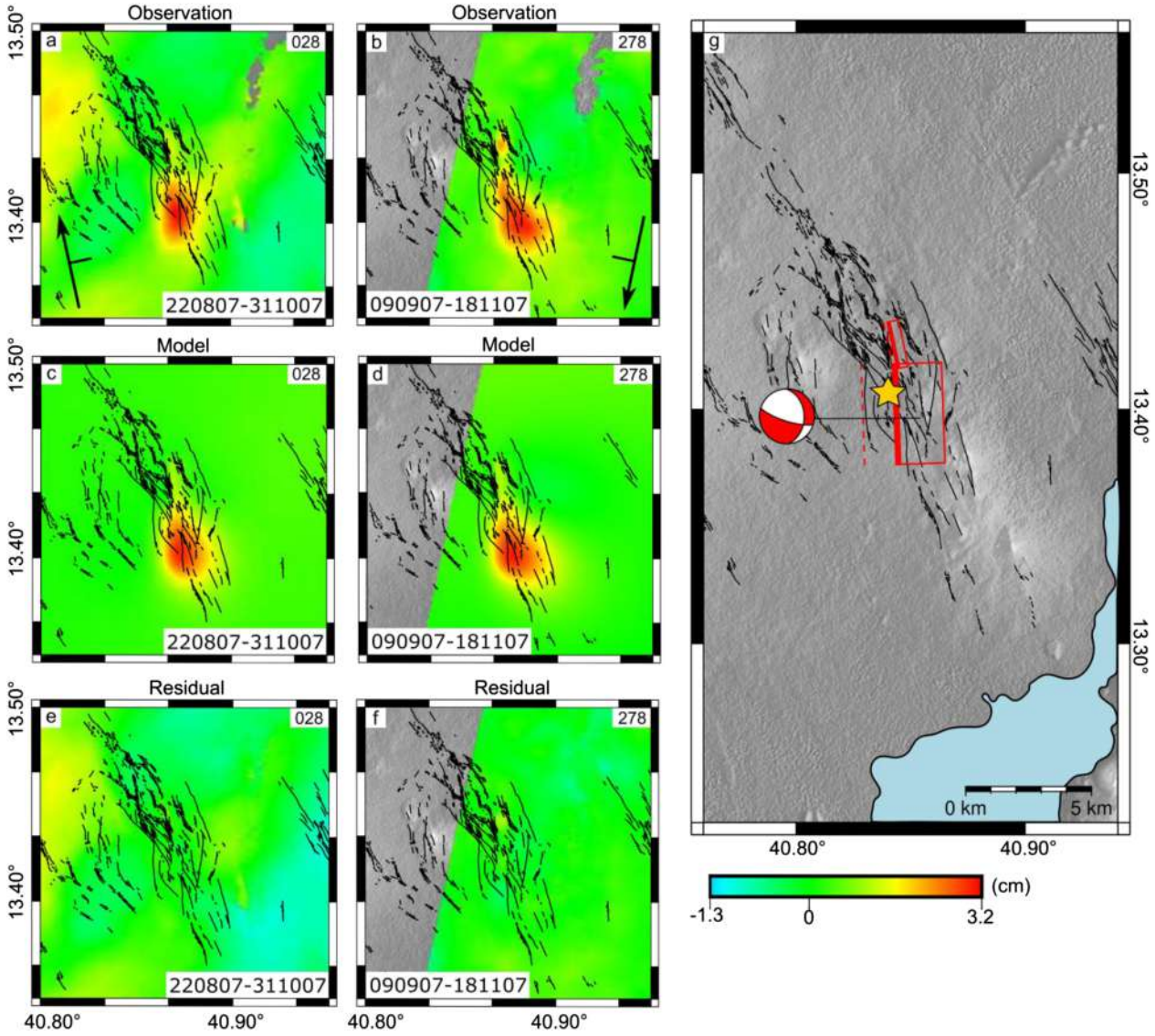

Figure 3. InSAR best fit model assuming two faults. (a) Observed ascending unwrapped interferogram. (b) Observed descending unwrapped interferograms. (c) Modeled ascending interferogram. (d) Modeled descending interferogram. (e) Residual ascending interferogram. (f) Residual descending interferogram. Tracks numbers are in the top right corner, dates of first and second satellite acquisitions are given at the bottom, and all interferograms are overlapped with faults (black lines) as in Figure 1b. (g) Outlines of the modeled faults in map view (red boxes). The thick red line marks the upper edge of the fault and the red dashed lines are the faults projections at surface. The red beach ball is the focal mechanism based on the best fit InSAR model. The location of the earthquake on 2 October 2007 from seismicity relocation is marked by a star.

of sight. A second smaller lobe is also present to the north of the main lobe and it displays ~1.5 cm of range increase (line of sight). The elongation of the lobes in the interferograms agrees well with the ~NS orientation of faults in AP (Figures 3 and S2), suggesting a fault slip along a NS striking structure. Furthermore, the preseismic and postseismic interferograms do not show any significant deformation before and after the earthquake on 2 October 2007, indicating that the deformation measured by InSAR (Figures 3 and S2) is coseismic.

2.3. Modeling

We inverted the InSAR data assuming an Okada rectangular shear dislocation model with uniform slip and assuming a homogeneous, elastic half-space with a Poisson's ratio of 0.25 and a shear modulus (μ) of 3.2×10^{10} Pa (Okada, 1992). For the modeling, we jointly inverted three independent interferograms,

selecting the ones with the lowest level of noise (tracks 028, 278, 464). Before the inversion, we subsampled the interferograms using a quadtree algorithm based on the data variance (Figure S3) (; Jonsson et al., 2002). To estimate the best fit parameters of the model, we used a nonlinear inversion consisting of a simulated annealing algorithm, followed by a derivative-based procedure (Cervelli et al., 2001). The inversion finds the best fit model by minimizing the weighted misfit between the data and the model predictions. We estimate the weight matrices using a one-dimensional covariance function to approximate the noise in each interferogram (Hanssen, 2001; Parsons et al., 2006). We also solved for a planar correction to remove any residual orbital errors. In the inversion, we set relatively large bounds on the fault parameters to explore a wide range of solutions. In particular we let the strike vary from N270°E to N20°E. The bounds on the dip angle were set 20°–90° while the length of the fault was free to change 1–7 km.

We also estimated the uncertainties on the fault parameters using a Monte Carlo simulation of correlated noise (Wang et al., 2014; Wright et al., 2003). We generated 100 simulations of the spatially correlated random noise based on the variance-covariance matrices of each interferogram. These noise simulations were added to observed data and then inverted, and the uncertainty on each fault parameter was estimated from the distribution of the model solutions. The results of the 100 nonlinear inversions and the uncertainties on the model parameters are shown in Figures S4 and S5.

Our best fit solution consists of two fault segments where slip is primarily accommodated by a ~3.9-km-long and ~2.4-km-wide fault, striking N358°E and dipping ~37° to the east. A second smaller ~1.8-km-long fault also accommodates some slip north of the main fault. The main fault has 4.6 cm of normal dip slip and 10.3 cm of left-lateral strike slip (Figure 3g and Table S2). The main fault geometry is rather well constrained with the length and width showing narrow 90% confidence intervals (C.I.) of 3.6–4.2 and 1.5–3.5 km, respectively. Strike-slip and normal components also have narrow 90% C.I. of 7.5–13.9 and 3.5–7.1 cm, respectively, while the dip is less well constrained with values ranging between 29° and 45° (Table S3). The second, smaller fault segment also has kinematics similar to the main fault with dominant normal dip slip of 4.7 and 1.3 cm of left-lateral strike slip (Tables S2 and S4 and Figure S5). Our best fit model has a total RMS of 4 mm and it gives a geodetic moment of 3.6×10^{16} Nm corresponding to a M_w 5 earthquake (Table S2), in excellent agreement with the CMT catalogue of M_w 5. Furthermore, our best fit fault model corresponds to mapped structures in the area and the oblique kinematics is similar to that of the focal mechanism from the CMT solution (Figure 1a).

We also considered other fault geometries to determine the correct earthquake parameters. In particular, we tested whether a model of the main fault with a steeper dip could be found by forcing the dip to vary between 65° and 90°. Although a fault model with a 65° dip can be found, the residuals are higher (Figure S6 and Table S5) compared to our preferred 37° dipping fault. Furthermore, the distribution of the model solutions assuming a steep fault dip, 65°–90°, has all the solutions clustering at the lower bound, 65° (Figure S7), hence showing that dip angles ≥65° are too steep. Instead the approximately normal distribution of the model solutions with dips between 29° and 45° (Figure S4 and Table S3) suggests that the best fit fault solution has a moderately shallow dip. Although this fault geometry is not fully Andersonian (Anderson, 1905), an explanation could be that the presence of preexisting weaknesses, such as other sets of faults as well as past eruptive fissures, influences the geometry and kinematics of the recent faults. These factors can explain why the Anderson theory may fail in predicting fault geometries in our study area (e.g., Bayerlee, 1978; Célériei, 2008; McKenzie, 1969).

We also tested a model of pure dip slip (Figure S9 and Table S6) as well as two faults corresponding to the nodal planes of the CMT solution (Table S7). For the CMT models we fixed the strike, dip, and rake and let the other parameters vary. The three models showed a worse fit to the data (Figures S9–S11) compared to our preferred model. In particular, the right-lateral fault model assuming the near E-W striking plane from the CMT solution has an unphysical geometry with a short and wide fault plane (Tables S8 and S9). We therefore prefer our first solution.

2.4. Seismicity Analysis

Seismicity in Afar was recorded by SEIS-UK and PASSCAL temporary seismic networks, from October 2005 to November 2009 (Belachew et al., 2011; Hammond et al., 2011). We have isolated 423 earthquakes from the AP during the time period of 14 July 2007 to 24 May 2008. For each earthquake, we manually picked a

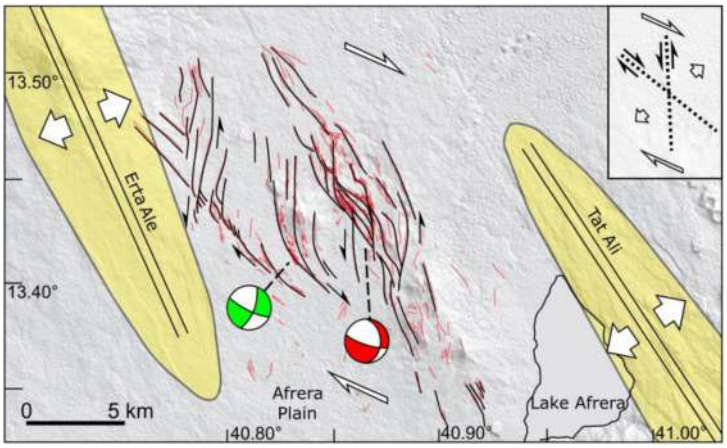

Figure 4. Kinematics of the Afrera Plain transfer zone. The red beach ball is the focal mechanism computed in this study based on InSAR inversion. The green beach ball is the focal mechanism reported in the area by Illsley-Kemp, Keir, et al. (2018).

minimum of four *P* and *S* wave arrivals to at least three seismic stations. Earthquakes have been then located using the Oct-Tree search algorithm implemented into the NLLoc software package (Lomax et al., 2000) and a two-dimensional velocity model based on the seismic refraction surveys of Makris and Ginzburg (1987).

In general, we observed high horizontal errors (ERH > 4.0 km) for events recorded by only three stations. To improve our spatial resolution of locations, we therefore isolated 203 earthquakes recorded by at least four stations (Table S10), which have average horizontal errors of ±2.34 km. Most of the earthquakes are located in the top 1 km when we allow the inversion to solve for a best fit depth. Due to the relatively large azimuthal gap and 10–30-km distance between earthquakes and nearest station, we also tested our shallow locations by fixing the earthquake depths to a volume at 2–4-km depth, consistent with the fault depth achieved from InSAR modeling. These locations are very similar to those achieved by our original locations, strongly suggesting that the earthquakes are indeed in the shallow crust (Figure S12). Magnitudes have been estimated by measuring the peak-to-peak amplitude on simulated Wood-Anderson seismometers, and then using the distance correction for the Danakil region by Illsley-Kemp et al. (2017).

Our results show that earthquakes are mainly focused along the NNW trending fault zone previously identified with InSAR and structural analysis. The cumulative seismic moment curve (Figure 1c) shows that seismicity is characterized by periodic swarms of low-magnitude earthquakes ($M_L \geq 4.0$) such as that accompanying the major event. The main seismic sequence lasted from 1 to 6 October, with 75 events with $M_L \geq 2.0$. The main event has been relocated to the area of highest coseismic displacement (Figures 1b and 3g), with a 68% confidence interval of ±2.78 km.

3. Discussion and Conclusion

Using a multidisciplinary set of structural, seismic, and InSAR data we observe the tectonic processes occurring in the AP linkage zone between the EA and TA segments in northern Afar. The faults and fissures in EA and TA strike N330°E and N328°E, respectively. GPS measurements show an ~N60°E regional extension direction (McClusky et al., 2010), strongly suggesting that rifting is orthogonal to the strike of the rift segments. Conversely, the AP shows a structural pattern consistent with a different strain field. Faults at AP have orientations varying between NNW-SSE and N-S with an average trend of ~N340°E. In the northern part of AP, we found evidence for coexisting left-lateral shear and normal faulting such as lozenge-shaped structures (Figure 4). These structures are predicted to form in oblique extensional settings by analogue models (e.g., McClay et al., 2002). To the south of AP, field measurements on horsetail fractures revealed local horizontal displacements with an average direction of N47°E, hence oblique with respect to the average strike of the fractures, N332°E.

Our relocated seismicity between 2007 and 2008 shows that earthquakes cluster along the main fault system and most of them occur in the area of highest coseismic displacement (Figure S13). Illsley-

Kemp, Bull, et al., 2018, Illsley-Kemp, Keir, et al., 2018) observed swarms of seismicity in the same area during 2011–2013. The authors also interpreted focal mechanisms computed using low-magnitude earthquakes as evidence of oblique right-lateral faulting along NW striking faults and concluded that these structures accommodate the deformation at AP while the NS striking faults are inactive. However, our best fit InSAR model shows that the deformation caused by the M_L 5 earthquake on 2 October 2007 occurred on ~NS striking faults with oblique left-lateral motions. Furthermore, the direction of maximum extension of our best fit InSAR model is N50°E, in agreement with the opening direction measured in the field of N47°E.

The structural data and our best fit model of the M_L 5 earthquake show that the strain at AP is primarily accommodated by left-lateral oblique slip along ~N-S striking faults. The right-lateral oblique slip along NW-SE trending faults (Illsley-Kemp, Keir, et al., 2018) likely represents a conjugate fault population, as commonly observed in shear zones (e.g., Davis et al., 2000; Dooley & Schreurs, 2012; Sibson, 1996). The occurrence of two conjugate fault systems can be explained by a model of plate boundary kinematics where two rift segments, TA and EA, are linked by an oblique right-lateral transfer zone (Figure 4). Analogue and numerical models of rift linkage zones show that at propagating rifts rotations of the extension direction occurs which leads to oblique slip (e.g., Allken et al., 2011, 2013; Corti et al., 2003; Le Pourhiet et al., 2017). Our observations at AP are consistent with counterclockwise rotation of the extension due to the formation of a transfer zones where strain is accommodated primarily by left-lateral oblique faults striking approximately parallel to the connecting EA and TA segments, while the conjugate NW-SE trending right-lateral faults are a secondary feature (Figure 4).

We also considered other models that could explain our data. In particular the bookshelf faulting model has been used to explain shear between segments in both southern and northern Iceland (Einarsson, 2008; Green et al., 2014), as this model can generate transfer zones with faults subparallel to the rift segments, as observed at AP. However, the bookshelf model predicts pure strike slip, which is not consistent with our observations of oblique tectonics and range of fault strikes. In contrast, Pagli et al. (2018) recently demonstrated that linkage between the Red Sea and the Gulf of Aden rifts in central Afar occurs through distributed extension in a series of rift-parallel and en echelon basins, driving rift-perpendicular shearing at the rift tips. Our results do not fit this model either, and instead provide the first direct observational evidence that offset rift segments during continental breakup can be linked by a shear zone composed of a conjugate set of oblique slip faults. These results contribute to the now growing body of observations for a wide variety of strain types that can link rift segments.

Acknowledgments
A.L.R. and C.P. acknowledge support by the University of Pisa grant PRA_2018_19. D.K. is supported by Natural Environment Research Council grant NE/L013932/1. F.S. acknowledges funding from MIUR FFABR2017. We also acknowledge PRIN2017 grant 2017P9AT72. H.W. is supported by the NSFC grant (41672205). The seismic data used in this study are provided by IRIS at https://ds.iris.edu/ds/nodes/dmc/forms/breqfast-request/. The facilities of IRIS Data Services, and specifically the IRIS Data Management Center, were used for access to waveforms. Envisat ASAR data are provided by the ESA Online Dissemination and are available at https://esar-ds.eo.esa.int/oads/access/.

References

Acocella, V., & Korme, T. (2002). Holocene extension direction along the Main Ethiopian Rift, East Africa. *Terra Nova*, *14*(3), 191–197. https://doi.org/10.1046/j.1365-3121.2002.00403.x

Allken, V., Huismans, R. S., Fossen, H., & Thieulot, C. (2013). 3D numerical modelling of graben interaction and linkage: A case study of the Canyonlands grabens, Utah. *Basin Research*, *25*(4), 436–449. https://doi.org/10.1111/bre.12010

Allken, V., Huismans, R. S., & Thieulot, C. (2011). Three-dimensional numerical modelling of upper crustal extensional systems. *Journal of Geophysical Research*, *116*, B10409. https://doi.org/10.1029/2011JB008319

Anderson, E. M. (1905). The dynamics of faulting. *Transactions of the Geological Society of Edinburgh*, *8*, 393–402. https://doi.org/10.1144/transed.8.3.387

Barberi, F., & Varet, J. (1970). The Erta Ale volcanic range (Danakil depression, northern Afar, Ethiopia). *Bulletin Volcanologique*, *34*(4), 848–917. https://doi.org/10.1007/BF02596805

Bayerlee, J. (1978). Friction of rocks. *Pure and applied geophysics*, *116*(4-5), 615–626. https://doi.org/10.1007/BF00876528

Belachew, M., Ebinger, C., Coté, D., Keir, D., Rowland, J. V., Hammond, J. O. S., & Ayele, A. (2011). Comparison of dike intrusions in an incipient seafloor-spreading segment in Afar, Ethiopia: Seismicity perspectives. *Journal of Geophysical Research*, *116*, B06405. https://doi.org/10.1029/2010JB007908

Beyene, A., & Abdelsalam, M. G. (2005). Tectonics of the Afar Depression: A review and synthesis. *Journal of African Earth Sciences*, *41*(1–2), 41–59. https://doi.org/10.1016/j.jafrearsci.2005.03.003

Bonatti, E., Gasperini, E., Vigliotti, L., Lupi, L., Vaselli, O., Polonia, A., & Gasperini, L. (2017). Lake Afrera, a structural depression in the northern Afar Rift (Red Sea). *Heliyon*, *3*(5), e00301. https://doi.org/10.1016/j.heliyon.2017.e00301

Célériei, B. (2008). Seeking Anderson's faulting in seismicity: A centennial celebration. *Reviews of Geophysics*, *46*, RG4001. https://doi.org/10.1029/2007RG000240

Cervelli, P., Murray, M. H., Segall, P., Aoki, Y., & Kato, T. (2001). Estimating source parameters from deformation data, with an application to the March 1997 earthquake swarm off the Izu Peninsula, Japan. *Journal of Geophysical Research*, *106*(B6), 11,217–11,237. https://doi.org/10.1029/2000JB900399

Corti, G., Bonini, M., Conticelli, S., Innocenti, F., Manetti, P., & Sokoutis, D. (2003). Analogue modelling of continental extension: A review focused on the relations between the patterns of deformation and the presence of magma. *Earth-Science Reviews*, *63*(3–4), 169–247. https://doi.org/10.1016/S0012-8252(03)00035-7

Davis, G. H., Bump, A. P., García, P. E., & Ahlgren, S. G. (2000). Conjugate Riedel deformation band shear zones. *Journal of Structural Geology*, *22*(2), 169–190. https://doi.org/10.1016/S0191-8141(99)00140-6

Dooley, T. P., & Schreurs, G. (2012). Analogue modelling of intraplate strike-slip tectonics: A review and new experimental results. *Tectonophysics*, *574-575*, 1–71. https://doi.org/10.1016/j.tecto.2012.05.030

Ebinger, C. J., Keir, D., Ayele, A., Calais, E., Wright, T. J., Belachew, M., et al. (2008). Capturing magma intrusion and faulting processes during continental rupture: Seismicity of the Dabbahu (Afar) rift. *Geophysical Journal International*, *174*(3), 1138–1152. https://doi.org/10.1111/j.1365-246X.2008.03877.x

Einarsson, P. (2008). Plate boundaries, rift and transforms in Iceland. *Jokull*, *58*(August).

Farr, T. G., Rosen, P. A., Caro, E., Crippen, R., Duren, R., Hensley, S., et al. (2007). The Shuttle Radar Topography Mission. *Reviews of Geophysics*, *45*, RG2004. https://doi.org/10.1029/2005RG000183

Green, R. G., White, R. S., & Greenfield, T. (2014). Motion in the north Iceland volcanic rift zone accommodated by bookshelf faulting. *Nature Geoscience*, *7*(1), 29–33. https://doi.org/10.1038/ngeo2012

Grindlay, N. R., Fox, P. J., & MacDonald, K. C. (1991). Second-order ridge axis discontinuities in the south Atlantic: Morphology, structure, and evolution. *Marine Geophysical Researches*, *13*(1), 21–49. https://doi.org/10.1007/BF02428194

Hammond, J. O. S., Kendall, J. M., Stuart, G. W., Keir, D., Ebinger, C., Ayele, A., & Belachew, M. (2011). The nature of the crust beneath the Afar triple junction: Evidence from receiver functions. *Geochemistry, Geophysics, Geosystems*, *12*, Q12004. https://doi.org/10.1029/2011GC003738

Hanssen, R. F. (2001). *Radar interferometry: Data interpretation and error analysis*. Netherlands: Kluwer Academic Publishers. https://doi.org/10.1007/0-306-47633-9

Hayward, N. J., & Ebinger, C. J. (1996). Variations in the along-axis segmentation of the Afar. *Tectonics*, *15*(2), 244–257. https://doi.org/10.1029/95TC02292

Illsley-Kemp, F., Bull, J. M., Keir, D., Gerya, T. V., Pagli, C., Gernon, T., et al. (2018). Initiation of a proto-transform fault prior to seafloor spreading. *Geochemistry, Geophysics, Geosystems*, *19*, 4744–4756. https://doi.org/10.1029/2018GC007947

Illsley-Kemp, F., Keir, D., Bull, J. M., Ayele, A., Hammond, J. O. S., Kendall, J. M., et al. (2017). Local earthquake magnitude scale and *b*-value for the Danakil region of northern afar. *Bulletin of the Seismological Society of America*, *107*(2), 521–531. https://doi.org/10.1785/0120150253

Illsley-Kemp, F., Keir, D., Bull, J. M., Gernon, T. M., Ebinger, C., Ayele, A., et al. (2018). Seismicity during continental breakup in the Red Sea rift of northern Afar. *Journal of Geophysical Research: Solid Earth*, *123*, 2345–2362. https://doi.org/10.1002/2017JB014902

Jonsson, S., Zebker, H., Segall, P., & Amelung, F. (2002). M_w7.1 Hector Mine, California, earthquake, estimated from satellite radar and GPS measurements. *Bulletin of the Seismological Society of America*, *92*(4), 1377–1389. https://doi.org/10.1785/0120000922

Keir, D., Bastow, I. D., Pagli, C., & Chambers, E. L. (2013). The development of extension and magmatism in the Red Sea rift of Afar. *Tectonophysics*, *607*, 98–114. https://doi.org/10.1016/j.tecto.2012.10.015

Keir, D., Hamling, I. J., Ayele, A., Calais, E., Ebinger, C., Wright, T. J., et al. (2009). Evidence for focused magmatic accretion at segment centers from lateral dike injections captured beneath the Red Sea rift in Afar. *Geology*, *37*(1), 59–62. https://doi.org/10.1130/G25147A.1

Kim, Y. S., Peacock, D. C. P., & Sanderson, D. J. (2004). Fault damage zones. *Journal of Structural Geology*, *26*(3), 503–517. https://doi.org/10.1016/j.jsg.2003.08.002

Le Pourhiet, L., May, D. A., Huille, L., Watremez, L., & Leroy, S. (2017). A genetic link between transform and hyper-extended margins. *Earth and Planetary Science Letters*, *465*, 184–192. https://doi.org/10.1016/j.epsl.2017.02.043

Lomax, A., Virieux, J., Volant, P., & Berge-Thierry, C. (2000). Probabilistic earthquake location in 3D and layered models. In C. H. Thurber, & N. Rabinowitz (Eds.), *Advances in seismic event location*, (pp. 101–134). Berlin: Springer. https://doi.org/10.1007/978-94-015-9536-0_5

Macdonald, K. C., Fox, P. J., Perram, L. J., Eisen, M. F., Haymon, R. M., Miller, S. P., et al. (1988). A new view of the mid-ocean ridge from the behaviour of ridge-axis discontinuities. *Nature*, *335*(6187), 217–225. https://doi.org/10.1038/335217a0

Makris, J., & Ginzburg, A. (1987). The Afar Depression: Transition between continental rifting and sea-floor spreading. *Tectonophysics*, *141*(1–3), 199–214. https://doi.org/10.1016/0040-1951(87)90186-7

McClay, K. R., Dooley, T., Whitehouse, P., & Mills, M. (2002). 4-D evolution of rift systems: Insights from scaled physical models. *AAPG Bulletin*, *86*, 935–959. https://doi.org/10.1306/61EEDBF2-173E-11D7-8645000102C1865D

McClusky, S., Reilinger, R., Ogubazghi, G., Amleson, A., Healeb, B., Vernant, P., et al. (2010). Kinematics of the southern Red Sea-Afar Triple Junction and implications for plate dynamics. *Geophysical Research Letters*, *37*, L05301. https://doi.org/10.1029/2009GL041127

McKenzie, D. P. (1969). The relation between fault plane solutions for earthquakes and the directions of the principal stresses. *Bulletin of the Seismological Society of America*, *59*(2), 591–601.

Okada, Y. (1992). Internal deformation due to shear and tensile faults in a half-space. *Bulletin of the Seismological Society of America*, *82*(2), 1018–1040.

Pagli, C., Wang, H., Wright, T. J., Calais, E., & Lewi, E. (2014). Current plate boundary deformation of the Afar rift from a 3-D velocity field inversion of InSAR and GPS. *Journal of Geophysical Research: Solid Earth*, *119*, 8562–8575. https://doi.org/10.1002/2014JB011391

Pagli, C., Wright, T. J., Ebinger, C. J., Yun, S.-H., Cann, J. R., Ayele, A., & Barnie, T. (2012). Shallow axial magma chamber at the slow-spreading Erta Ale Ridge. *Nature Geoscience*, *5*(4), 284–288. https://doi.org/10.1038/NGEO1414

Pagli, C., Yun, S.-H., Ebinger, C., Keir, D., & Wang, H. (2018). Strike-slip tectonics during rift linkage. *Geology*, *47*(1), 31–34. https://doi.org/10.1130/g45345.1

Parsons, B., Wright, T., Rowe, P., Andrews, J., Jackson, J., Walker, R., et al. (2006). The 1994 Sefidabeh (eastern Iran) earthquakes revisited: New evidence from satellite radar interferometry and carbonate dating about the growth of an active fold above a blind thrust fault. *Geophysical Journal International*, *164*(1), 202–217. https://doi.org/10.1111/j.1365-246X.2005.02655.x

Rosen, P. A., Scont Hensley, G. P., & S, M. (2004). Updated Repeat Orbit Interferometry Package released. *Eos, Transactions, American Geophysical Union*, *85*(5). https://doi.org/10.1029/2004EO050004

Sibson, R. H. (1996). Structural permeability of fluid-driven fault-fracture meshes. *Journal of Structural Geology*, *18*(8), 1031–1042. https://doi.org/10.1016/0191-8141(96)00032-6

Wang, H., Elliott, J. R., Craig, T. J., Wright, T. J., Liu-Zeng, J., & Hooper, A. (2014). Normal faulting sequence in the Pumqu-Xainza Rift constrained by InSAR and teleseismic body-wave seismology. *Geochemistry Geophysics Geosystems*, *15*, 2947–2963. https://doi.org/10.1002/2014GC005369

Wetzel, L. R., Wiens, D. A., & Kleinrockt, M. C. (1993). Evidence from earthquakes for bookshelf faulting at large non-transform ridge offsets. *Nature*, *362*(6417), 235–237. https://doi.org/10.1038/362235a0DO

Wright, T. J., Lu, Z., & Wicks, C. (2003). Source model for the M_w 6.7, 23 October 2002, Nenana Mountain earthquake (Alaska) from InSAR. *Geophysical Research Letters*, *30*(18), 1974. https://doi.org/10.1029/2003GL018014

Wright, T. J., Sigmundsson, F., Pagli, C., Belachew, M., Hamling, I. J., Brandsdóttir, B., et al. (2012). Geophysical constraints on the dynamics of spreading centres from rifting episodes on land. *Nature Geoscience*, *5*(4), 242–250. https://doi.org/10.1038/ngeo1428